Supporting Information

Identifying Electrocatalytic Sites of Nanoporous Copper-Ruthenium Alloy for Hydrogen Evolution Reaction in Alkaline Electrolytes

Qiuli Wu, [†] *Min Luo,* [‡] *Jiuhui Han,* [§] *Wei Peng,* [†] *Yang Zhao,* [†] *Dechao Chen,* [†] *Ming Peng,* [†] *Ji Liu,* [†] *Frank M. F. de Groot,* [‖] *Yongwen Tan*[†]*

[†]College of Materials Science and Engineering, Hunan University, Changsha, Hunan 410082, China

[‡]Department of Physics, Shanghai Polytechnic University, Shanghai 201209, China

[§]Advanced Institute for Materials Research, Tohoku University, Sendai 980-8577, Japan

[‖] Inorganic Chemistry & Catalysis, Debye Institute for Nanomaterials Science, Utrecht University, Universiteitsweg 99, 3584 CG Utrecht, Netherlands

Experimental Section

Preparation of alloys of np-$Cu_{100-x}Ru_x$: The Ru-Cu-Mn ribbons were got by arc melting pure Ru, pure Cu and pure Mn under an argon atmosphere. The Ru: Cu: Mn atomic ratios were designed to fabricate precursor $Ru_3Cu_{22}Mn_{75}$. The ribbons were prepared by rapidly re-melt the alloy ingots the cold surface of a spinning copper roller with the width of 2 mm and the thickness of 40 μm. The Ru: Cu: Mn atomic ratios were determinated by EDS and ICP (**Figure S2 and Table S1**). The np-$Cu_{100-x}Ru_x$ (x =12, 47, 65) alloys with tunable Ru/Cu ratios were prepared by chemical dealloying the precursor for different time in 1 M $(NH_4)_2SO_4$ solution heating at 40°C.

Preparation of np-Cu: The preparation of the Cu-Mn ribbons is the same as the above process, but the precursor was $Cu_{25}Mn_{75}$. Then, $Cu_{25}Mn_{75}$ ribbons were dealloyed in 1 M $(NH_4)_2SO_4$ solution at 40°C for 48 hours. After dealloying, the np-Cu was obtained.

Characterization: XRD patterns of the samples were taken by using a Bruker D8 Advance X-ray diffraction (Cu Kα, λ=1.5418 Å). Microscopic morphology was performed with a Zeiss Sigma HD SEM at 10 kV. HAADF-STEM images were taken by a JEOL JEM-2100F operated at 200 kV. The chemical state of samples were tested using X-ray photoelectron spectroscopy (Thermo Scientific Escalab 250Xi with a Al Kα monochromatic). The content of Ru and Cu were obtained with the Agilent 730 (ICP-OES: inductively coupled plasma-optical emission spectrometer). The nitrogen adsorption isotherms were collected at 77 K (Micromeritics ASAP 2020) and the specific surface area was obtained by BET (Brunauer-Emmet-Teller) means. The *ex-situ* X-ray absorption spectroscopy (the Ru-K, and Cu K-edge XAS spectra of np-$Cu_{53}Ru_{47}$ and the Cu K-edge XAS spectra of np-Cu) was performed on Beamline BL01C1 at National Synchrotron Radiation Research Center (NSRRC, Taiwan). The data were operated in the fluorescence mode at room temperature (25°C). The *in-situ* XAFS data were obtained with the same condition to get atomic environment and valence state changes during the catalytic process. For the *in-situ* measurements (**Figure S20**), the diluted catalysts were evenly coated on the carbon cloth (0.4 mm in thickness), which was used as a working electrode. A graphite rod and a saturated calomel were used as counter electrode and reference electrode in 1.0 M KOH, respectively. A well-designed

polytetrafluoroethylene (PTFE) cell were used for the electrochemical process. The window of the PTFE cell was installed at about 45° towards incident beam and detector. The different potentials of OCV, -0.1V, -0.2 V and -0.3 V versus RHE were applied to the working electrode during the test.

Electrochemical measurements: The electrochemical tests were carried out an electrochemical workstation (Ivium CompactStat. h) with a three-electrode cell using a rotating disc electrode (RDE) at room temperature. A graphite rod and a Ag/AgCl electrode were used as the counter and reference electrode, respectively. All potentials refer to that of the reversible hydrogen electrode (RHE) after transformation ($E_{RHE} = E_{Ag/AgCl} + 0.0591$ pH + 0.197 V). The working electrodes for HER were made by applying catalyst ink onto the glassy carbon electrode (GCE) with an area of 0.196 cm^2. The catalyst inks were prepared by dispersing 2 mg powder in a solution containing 0.5 mL of ethanol and 15 μL of 5wt% Nafion solution by sonication for 1 hour. Then 15 μL ink was dropped on the GCE for drying in the air, and the loading mass of catalyst is 0.306 mg cm^{-2}. The polarization curves of HER were carried out in Ar-saturated 1.0 M PBS and 1.0 M KOH solution with a scan rate of 2 mV s^{-1} with the working electrode rotating at 1600 rpm to remove the bubbles on the electrode. All potentials were corrected with iR to the reversible hydrogen electrode (RHE), and EIS measurements were carried out from 0.01 to 10^6 Hz under operating voltage.

Faradaic efficiency measurements: Faradaic efficiency of np-$Cu_{53}Ru_{47}$ was measured with the cell as shown in **Figure S14** at applied potentials (-0.01, -0.05, -0.10, -0.15, -0.20 V vs RHE). The gas chromatography (GC-2014C, Shimadzu) has a thermal conductivity detector for H_2 quantification. Ultra pure argon (Ar, 99.999%) was used as the carrier gas. Nafion 117 membrane space out a customized two cells, and each compartment of the cell was filled with 35 mL 1.0 M KOH solution.

Calculation of the mass activity and price activity: For comparison the mass activities of Pt/C, Ru/C, np-$Cu_{53}Ru_{47}$, the activity values were normalized to mass loadings. For np-$Cu_{53}Ru_{47}$, the contributions of np-Cu have been deducted. The current density at -50 mV vs. RHE was applied to assess the mass activity. The details are as follows:[1]

$$j_{mass}^{np-Cu_{53}Ru_{47}} = \frac{j_{area}^{np-Cu_{53}Ru_{47}} - j_{area}^{np-Cu}\ (mA\ cm^{-2})}{mass_{Ru}} = \frac{34.530 - 0.003\ (mA\ cm^{-2})}{0.306 * 56.53\%\ (mg\ cm^{-2})}$$

$$= 199.599\ mA\ mg^{-1}$$

$$j_{mass}^{Pt/C} = \frac{j_{area}^{Pt/C}}{mass_{Pt}} = \frac{24.812\ (mA\ cm^{-2})}{0.306\ (mg\ cm^{-2})} = 81.085\ \ mA\ mg^{-1}$$

$$j_{mass}^{Ru/C} = \frac{j_{area}^{Ru/C}}{mass_{Ru}} = \frac{3.277\ (mA\ cm^{-2})}{0.306\ (mg\ cm^{-2})} = 10.709\ \ mA\ mg^{-1}$$

For comparison the price activities of Pt/C, Ru/C, and np-$Cu_{53}Ru_{47}$, through the above results, we obtained the mass activity of the prepared catalysts. Then, mass activity divided by their price (**Table S2**), respectively. The value obtained is the price activity.

$$j_{price}^{np-Cu_{53}Ru_{47}} = \frac{mass\ activity_{np-Cu_{53}Ru_{47}}}{price_{Ru}} = \frac{199.599\ (mA\ mg^{-1})}{195\ /28.3495(dollar\ g^{-1})} = 29.018\ \ A\ dollar^{-1}$$

$$j_{price}^{Pt/C} = \frac{mass\ activity_{Pt/C}}{price_{Pt}} = \frac{81.085\ (mA\ mg^{-1})}{974/28.3495(dollar\ g^{-1})} = 2.36\ A\ dollar^{-1}$$

$$j_{price}^{Ru/C} = \frac{mass\ activity_{Ru/C}}{price_{Pt}} = \frac{10.709\ (mA\ mg^{-1})}{195/28.3495(dollar\ g^{-1})} = 1.557\ A\ dollar^{-1}$$

Calculation of the active site density and TOF: In order to compute per-site turnover frequency (TOF) of catalysts, we learned from the reported method.[2, 3] The per-site TOF values can be computed according to the following equation:

$$TOF = \frac{Total\ number\ of\ hydrogen\ turnover/geometric\ area\ (cm^{-2})}{Number\ of\ active\ sites/geometric\ area\ (cm^{-2})}$$

The number of total hydrogen turnovers are calculated from the current density according to:

Number of hydrogens

$$= \left(j\frac{mA}{cm^2}\right)\left(\frac{1\ C\ s^{-1}}{1000\ mA}\right)\left(\frac{1\ mol\ e^{-1}}{96485.3\ C}\right)\left(\frac{1\ mol\ H_2}{2\ mol\ e^{-}}\right)\left(\frac{6.022 \times 10^{23} molecules\ H_2}{1\ mol\ H_2}\right)$$

$$= 3.12 \times 10^{15}\ H_2\ s^{-1} cm^{-2}\ per\ mA\ cm^{-2}$$

The active sites per real surface area are calculated from the following formula: [4]

$$\text{Number of active sites} = \left(\frac{No.of\ atoms/unit\ cell}{Volume/unit\ cell}\right)^{2/3}$$

$$\text{Number of active sites(Cu)} = \left(\frac{4\ atoms/unit\ cell}{41.237713Å^3/unit\ cell}\right)^{\frac{2}{3}} = 2.111 \times 10^{15} atoms\ cm_{real}^{-2}$$

$$\text{Number of active sites(Ru)} = \left(\frac{4\ atoms/unit\ cell}{41.237713Å^3/unit\ cell}\right)^{\frac{2}{3}} = 2.111 \times 10^{15} atoms\ cm_{real}^{-2}$$

Note that according to the XRD results (**Figure 1b**), np-$Cu_{53}Ru_{47}$ forms a solid solution alloy, and Ru is embedded in the crystal lattice of Cu. Therefore, the number of active sites of Ru is calculated according to the unit cell of Cu.

The active site density of Cu is estimated by using the method suggested by: [5]

$$np - Cu_{53}Ru_{47} : 2.111 \times 10^{15}\ atoms\ cm_{real}^{-2} \times (BET_2) \times (mass) = 1.015 \times 10^{17}\ Cu - sites\ cm^{-2}$$

Finally, the current density from the LSV polarization curve can be transformed into TOF values based on: [1]

$$TOF_{np-Cu_{53}Ru_{47}} = \frac{3.12 \times 10^{15}\ H_2\ s^{-1}\ cm^{-2}\ per\ mA\ cm^{-2}}{1.015 \times 10^{17}\ Ru - sites\ cm^{-2} + 1.015 \times 10^{17}\ Cu - sites\ cm^{-2}} \times j = 0.015\ j$$

Therefore, the TOF values of np-$Cu_{53}Ru_{47}$ catalyst was calculated to be:

TOF (-0.1 V vs. RHE) = 1.139 H_2 s^{-1}

Calculation of the electrochemically active surface areas (ECSA):

The real surface area for HER is calculated from the electrochemical active surface area (ECSA), which can be converted from the specific capacitance[4]. The specific capacitance for a flat surface is generally found to be in the range of 20-60 μF cm^2_{geo}.

$$A_{ECSA} = \frac{specific\ capacitance}{60\ \mu F\ cm^2_{geo} per\ cm^2_{ECSA}}$$

From **Figure S12** we can calculate ECSA for np-$Cu_{53}Ru_{47}$ and np-Cu:

$$A_{ECSA}(np - Cu_{53}Ru_{47}) = \frac{59\ mF\ cm^{-2}}{60\ \mu F\ cm^2_{geo} per\ cm^2_{ECSA}} = 983.3\ cm^2_{ECSA}$$

$$A_{ECSA}(np - Cu) = \frac{8.5\ mF\ cm^{-2}}{60\ \mu F\ cm^2_{geo} per\ cm^2_{ECSA}} = 141.7\ cm^2_{ECSA}$$

Theoretical calculations: All the density functional theory (DFT) calculations were used by Vienna Ab-initio Simulation Package (VASP).[6, 7] The spin-polarized projector augmented wave (PAW) projectors

and the Perdew-Burke-Ernzerhof (PBE) functional of generalized gradient approximation (GGA) was applied to depict the electronic structures of catalysts.[8, 9] The DFT-D3 empirical correction method was used to accurately describe the van der Waals interactions. The energy cut off for the plane-wave expansion was established to 400 eV. The energy convergence was established to 10^{-5} eV, and the residual force on each atom was smaller than 0.01 eV/Å for structural relaxations. For $Cu_{50}Ru_{50}$ model, we replaced Cu atoms with Ru atoms in the (4 × 4 × 3) supercell. For the slab models of pure Cu and Ru, we chose (001) surface with different termination and 3 × 3 repeated unit cell and three atom layers.

Supporting Figures

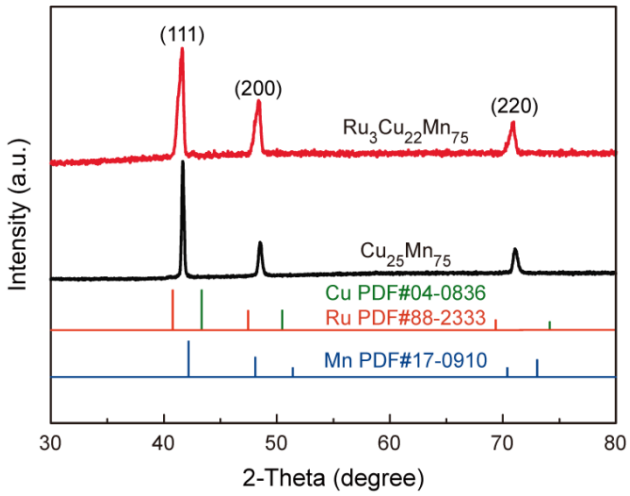

Figure S1. XRD pattern of $Ru_3Cu_{22}Mn_{75}$ and $Cu_{25}Mn_{75}$ precursors. There are three main peaks, which can be assigned to (1 1 1), (2 0 0) and (2 2 0) diffraction of a single-phase face-centered cubic (FCC) structure.

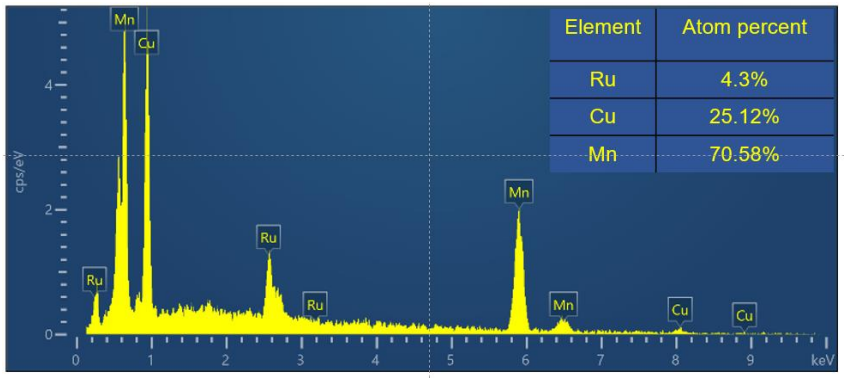

Figure S2. EDS spectra of the as-synthesized precursor ($Ru_3Cu_{22}Mn_{75}$).

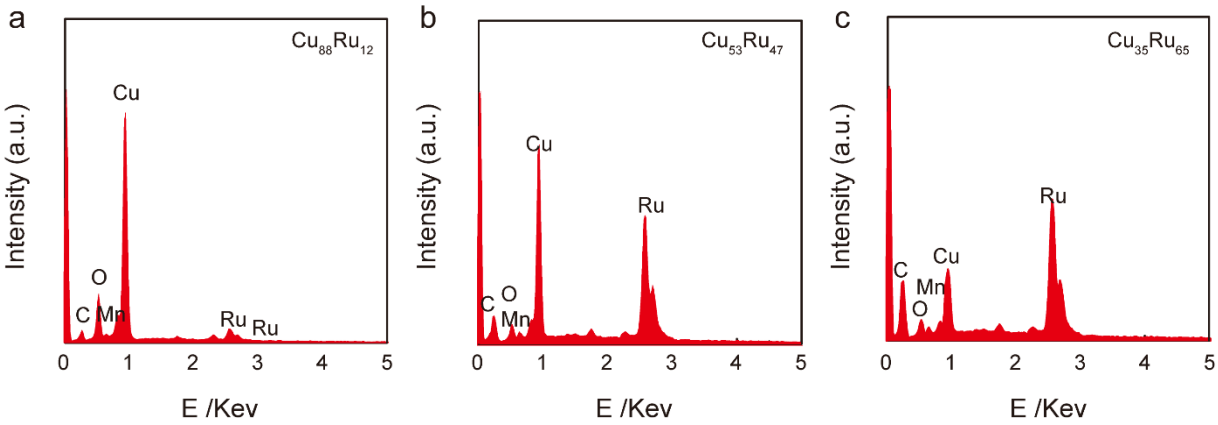

Figure S3. EDS patterns of the np-$Cu_{100-x}Ru_x$ (x = 12, 47, 65) alloys: (a) np-$Cu_{88}Ru_{12}$, (b) np-$Cu_{53}Ru_{47}$, (c) np-$Cu_{35}Ru_{65}$.

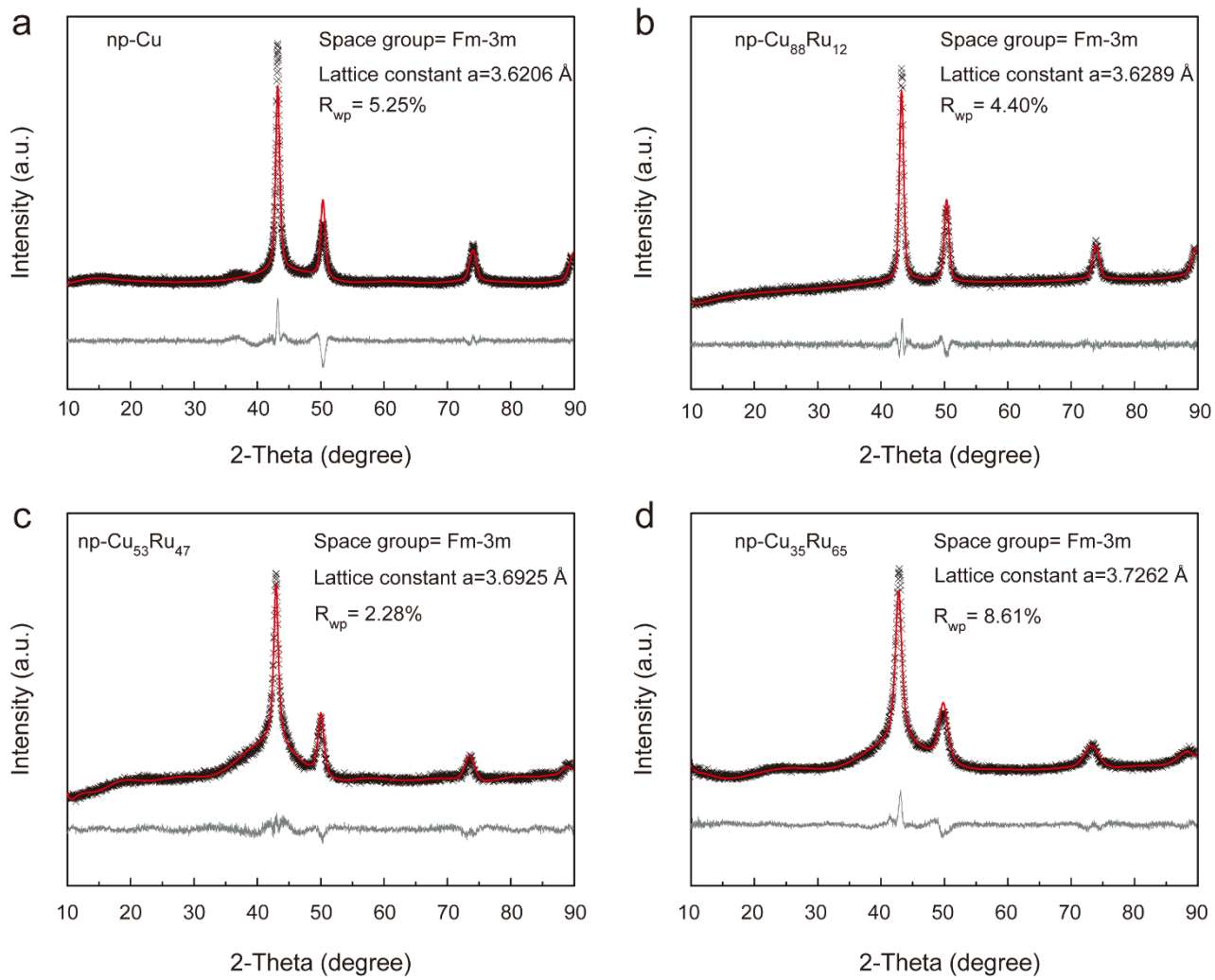

Figure S4. XRD patterns obtained on the observed catalysts (black) and the calculated curve (red). The below line shows the difference profile (gray). (a) np-Cu, (b) np-$Cu_{88}Ru_{12}$, (c) np-$Cu_{53}Ru_{47}$, (d) np-$Cu_{35}Ru_{65}$. The lattice constant of np-Cu, np-$Cu_{100-x}Ru_x$ (x = 12, 47, 65) were estimated to be 3.621, 3.629, 3.692 and 3.726 Å, respectively. These results indicate the formation of the FCC np-$Cu_{100-x}Ru_x$ (x = 12, 47, 65) alloy.

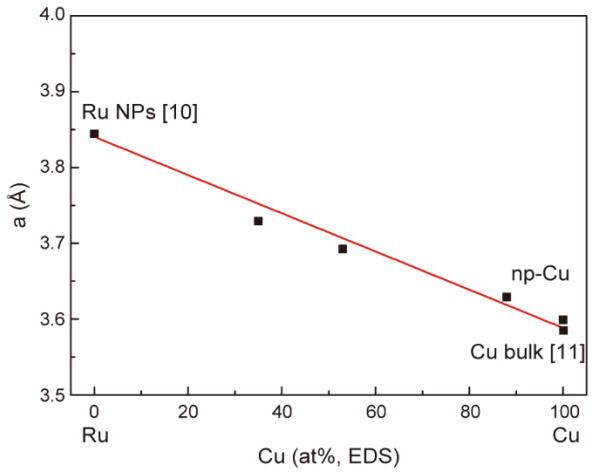

Figure S5. Correlation between the calculated lattice constants and the metal compositions of np-$Cu_{100-x}Ru_x$ (x=12, 47, 65). (The metal content in the alloy was determined by EDS)

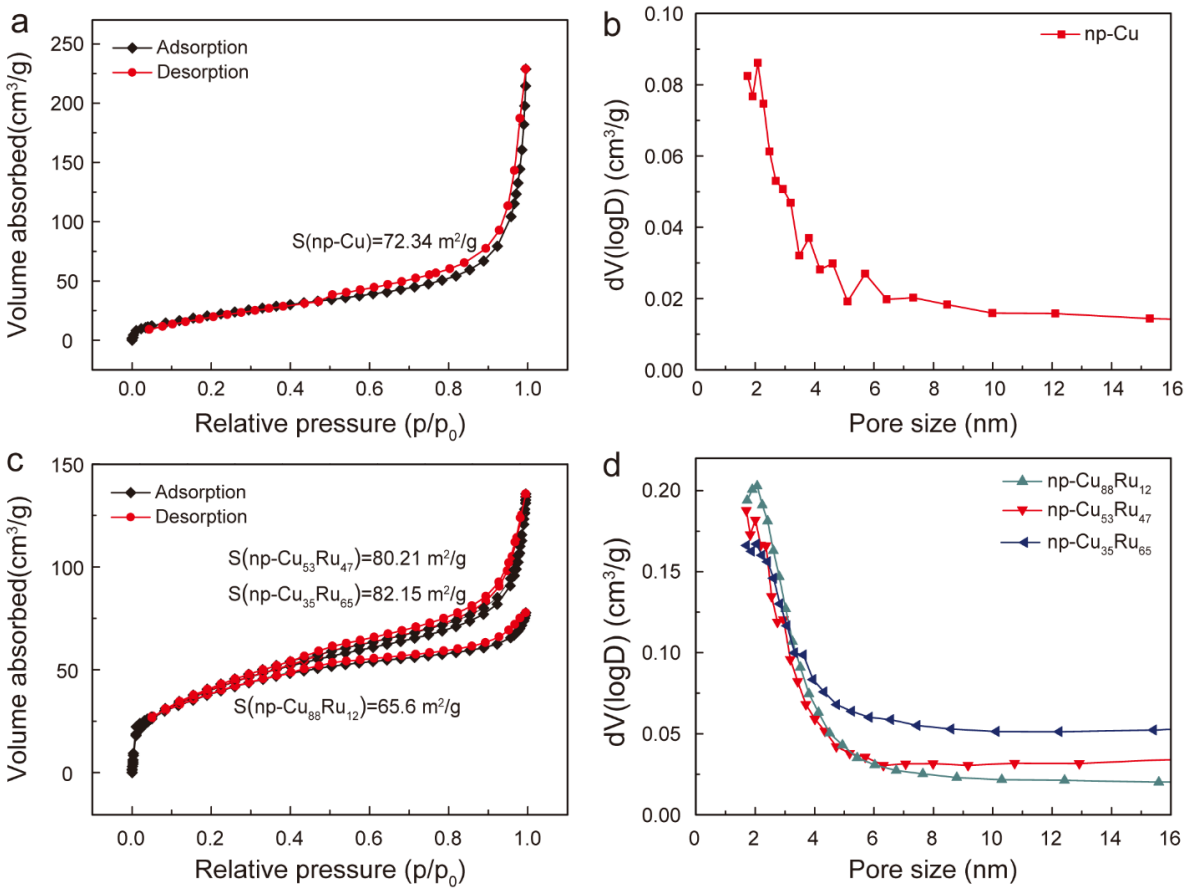

Figure S6. (a.c) Nitrogen adsorption/desorption curve of np-Cu and np-$Cu_{100-x}Ru_x$(x=12, 47,65). (b.d) Pore size distribution of np-Cu and np-$Cu_{100-x}Ru_x$ (x=12, 47,65). The range of relative pressure is from 0 to 1.

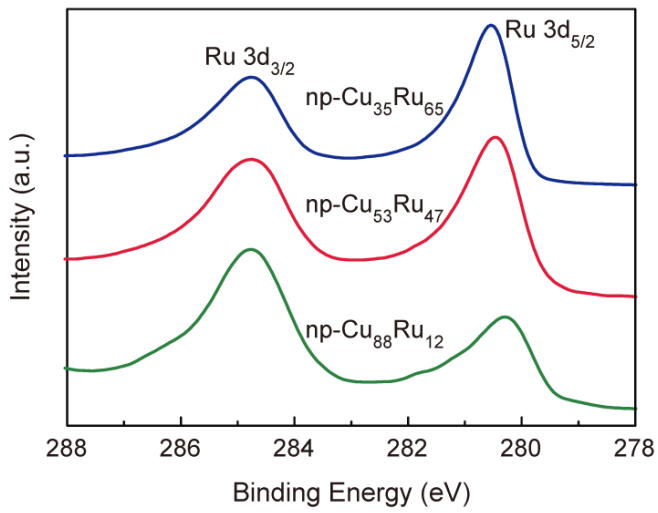

Figure S7. Ru 3d core-level XPS spectra recorded on np-$Cu_{88}Cu_{12}$, np-$Cu_{53}Ru_{47}$, and np-$Cu_{35}Ru_{65}$.

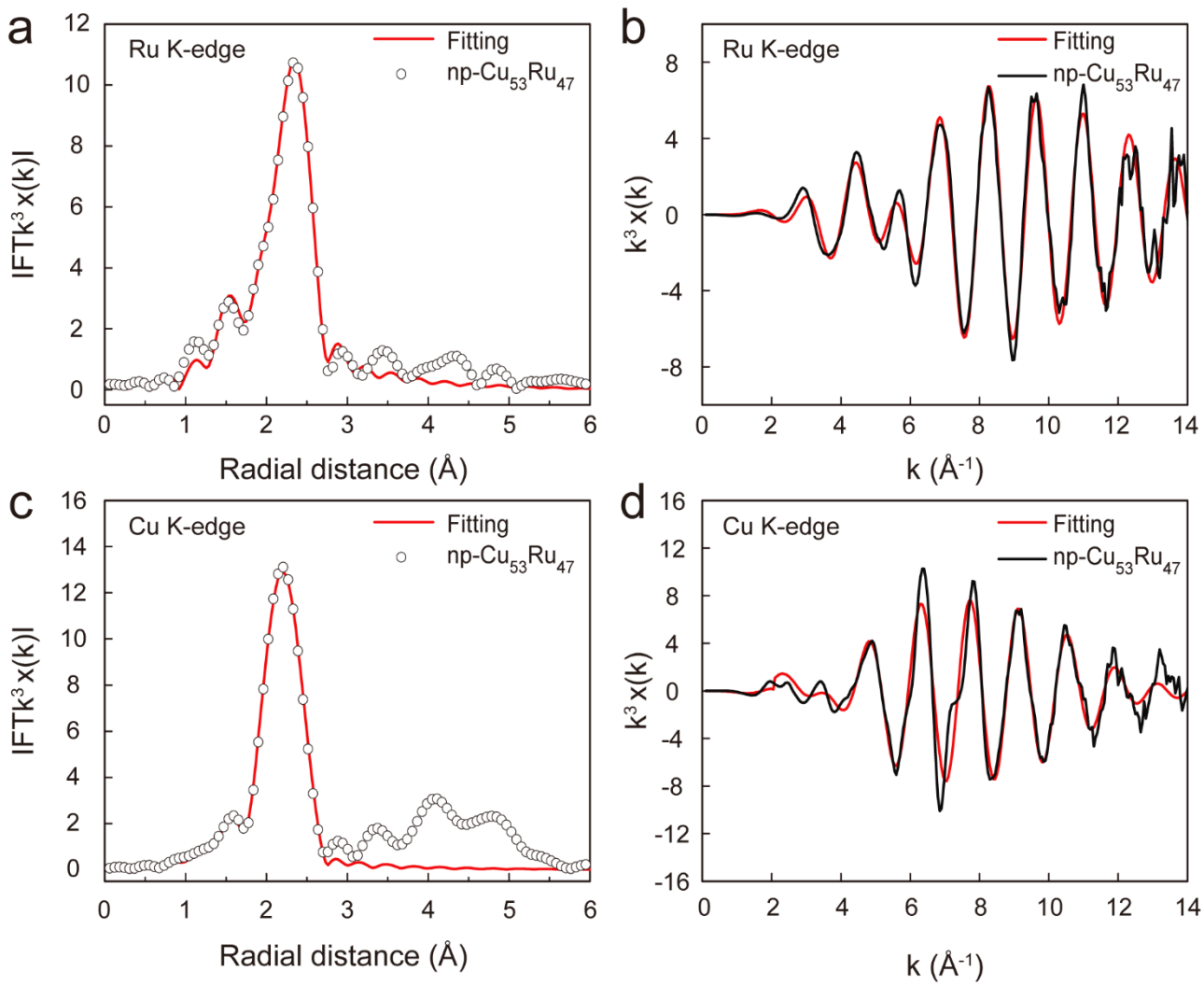

Figure S8. R space and inverse FT-EXAFS fitting of np-$Cu_{53}Ru_{47}$. (a) (b) R space and inverse FT-EXAFS fitting result of Ru K-edge. (c)(d) R space and inverse FT-EXAFS fitting result of Cu K-edge.

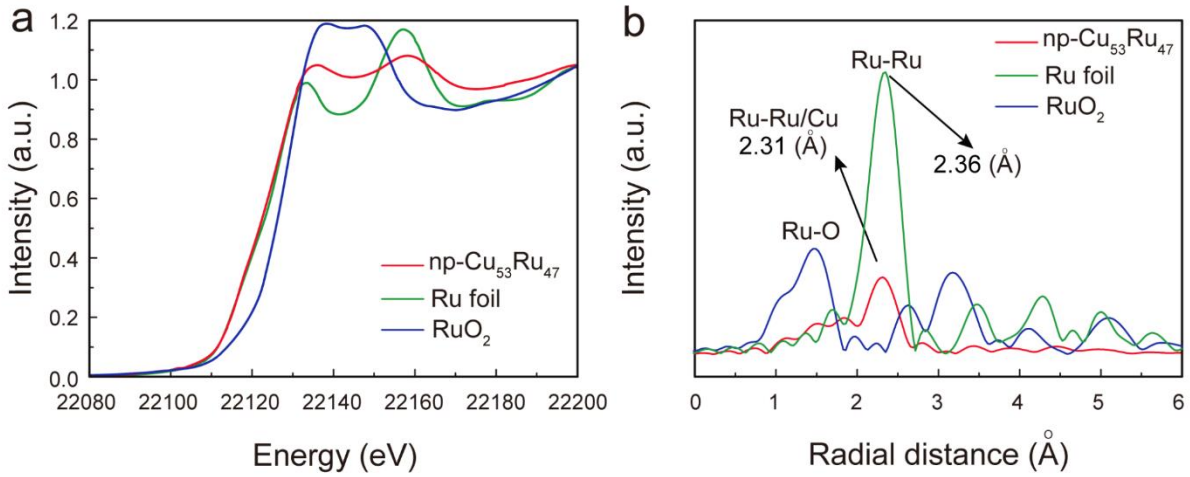

Figure S9. (a) The normalized XANES at the Ru K-edge of np-$Cu_{53}Ru_{47}$, Ru foil, RuO_2. (b) The FT k^3-edge weighted c(k)-function of the EXAFS spectra for the Ru K-edge.

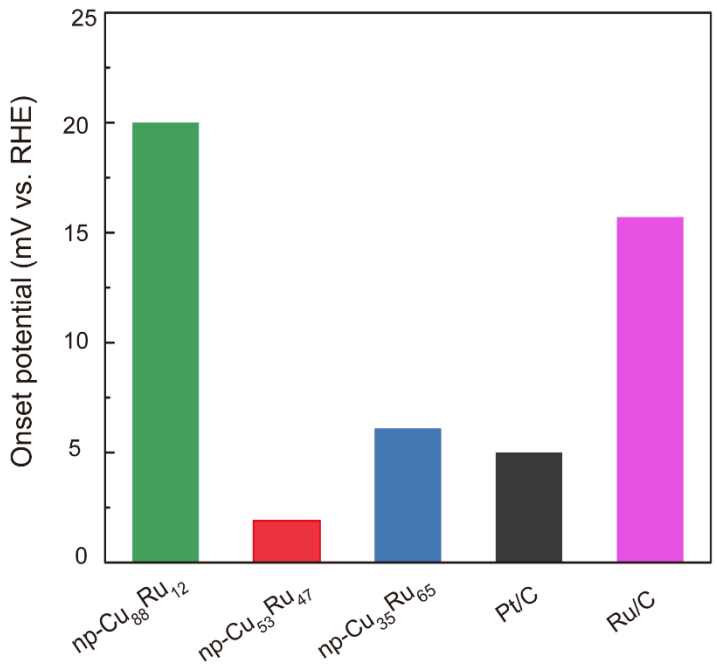

Figure S10. Onset potential at −1 mA cm^{-2} of np-$Cu_{88}Ru_{12}$, np-$Cu_{53}Ru_{47}$, np-$Cu_{35}Ru_{65}$, Pt/C and Ru/C in 1.0 M KOH.

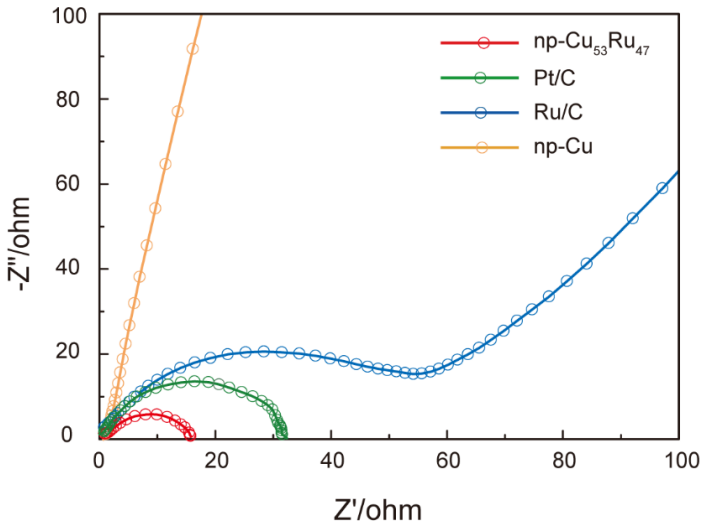

Figure S11. Electrochemical impedance spectroscopy (EIS) of np-$Cu_{53}Ru_{47}$, Pt/C, Ru/C and np-Cu catalysts in 1.0 M KOH. EIS measurement was performed at -0.15 V vs. RHE.

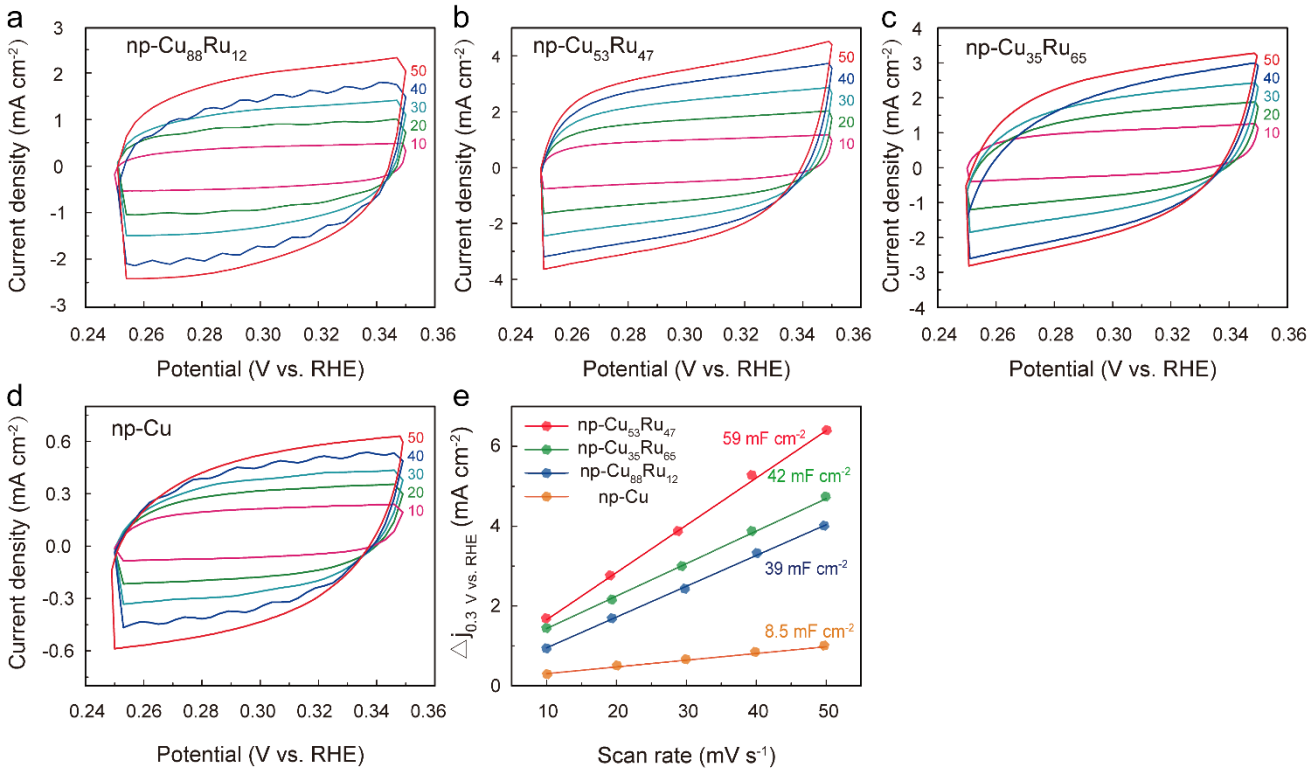

Figure S12. CVs of (a-d) np-$Cu_{88}Ru_{12}$, np-$Cu_{53}Ru_{47}$, np-$Cu_{35}Ru_{65}$, and np-Cu. These CVs were performed at various scan rates (10, 20, 30, 40, and 50 mV s^{-1}). (e) The plots of current densities against scan rates. Δj is the difference between anodic and cathodic current densities at a same potential (0.3 V vs. RHE).

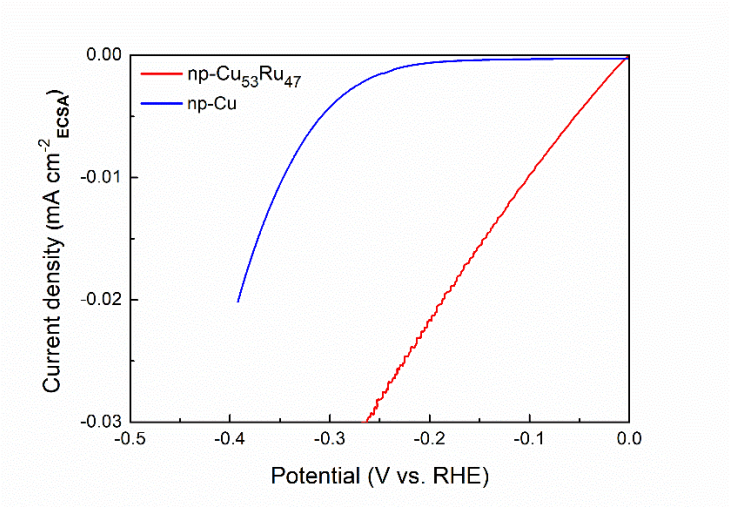

Figure S13. Polarization curves of different samples normalized by the ECSA.

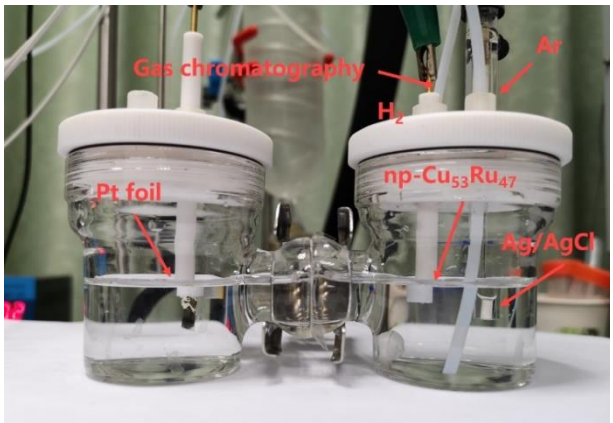

Figure S14. The electrochemical cell for Faradaic efficiency measurement.

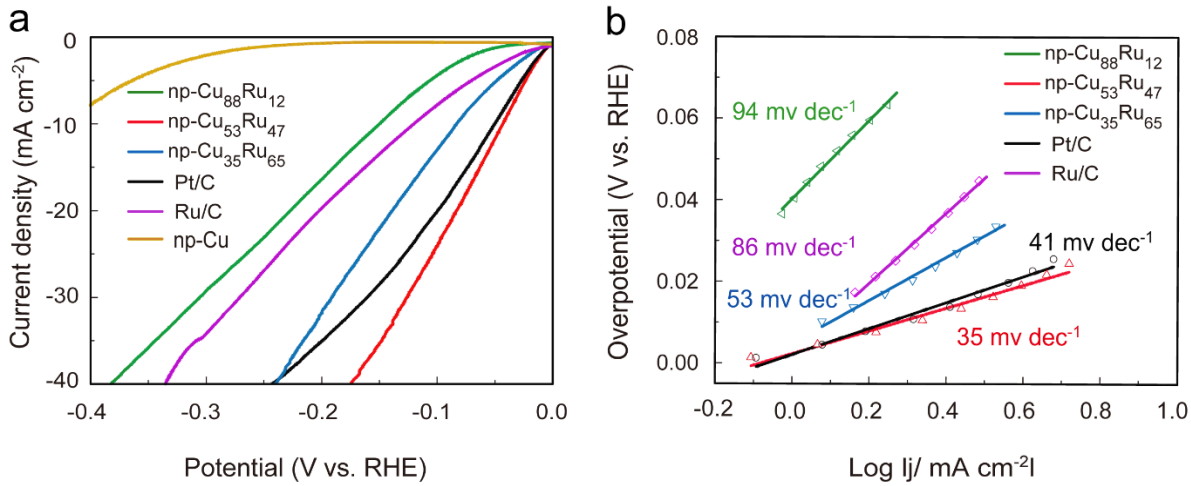

Figure S15. (a) Polarization curves and (b) Tafel plots of np-$Cu_{88}Ru_{12}$, np-$Cu_{53}Ru_{47}$, and np-$Cu_{35}Ru_{65}$ for HER with iR-compensation in 1.0 M PBS.

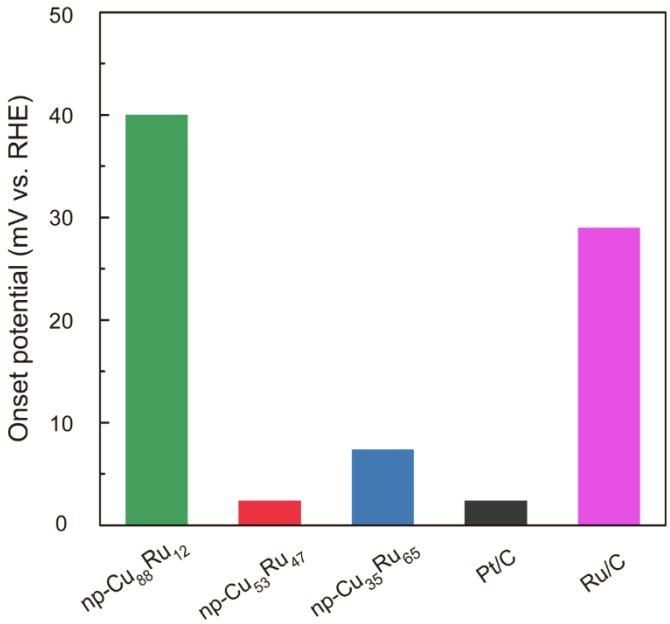

Figure S16. Onset potential at −1 mA cm^{-2} of np-$Cu_{88}Ru_{12}$, np-$Cu_{53}Ru_{47}$, np-$Cu_{35}Ru_{65}$, Pt/C and Ru/C in neutral solution.

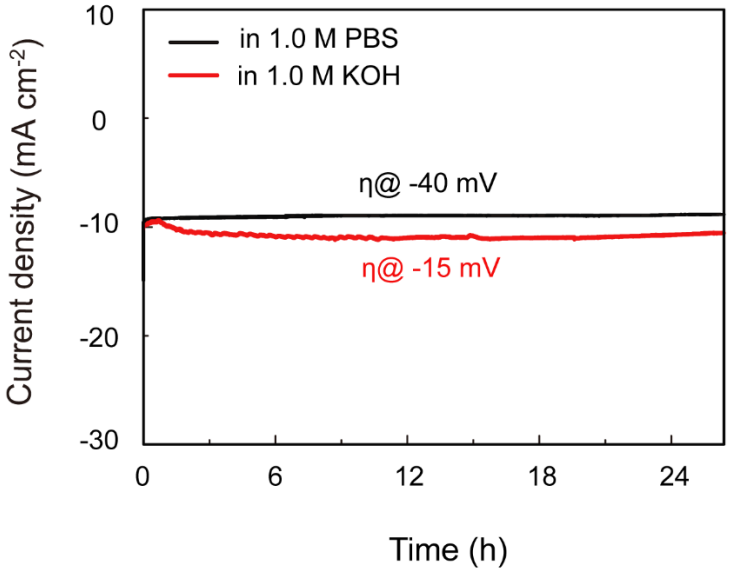

Figure S17. Time-dependent current density curves (I–t curve) under static overpotential for np-$Cu_{53}Ru_{47}$ in alkaline (red) and neutral solution (black).

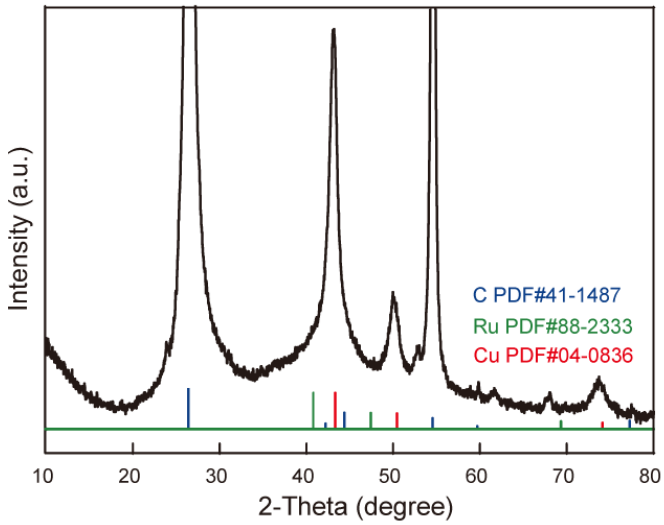

Figure S18. XRD pattern of np-$Cu_{53}Ru_{47}$ after long-term chronoamperometric testing. The sharp C peaks in the XRD pattern is from the carbon paper as a support of the catalyst.

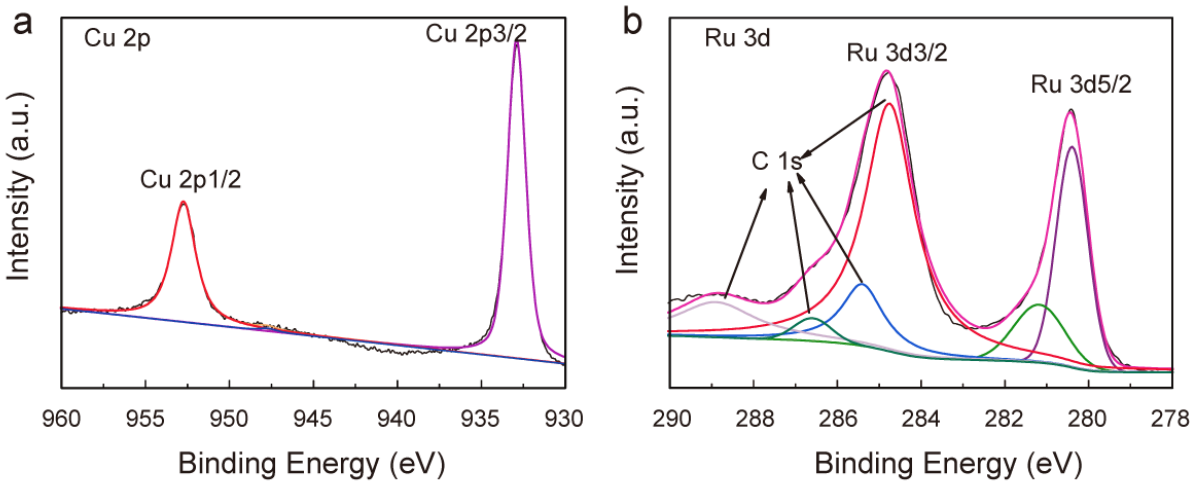

Figure S19. The Cu 2p (a) and Ru 3d (b) XPS spectra of the np-$Cu_{53}Ru_{47}$ after long-term chronoamperometric testing.

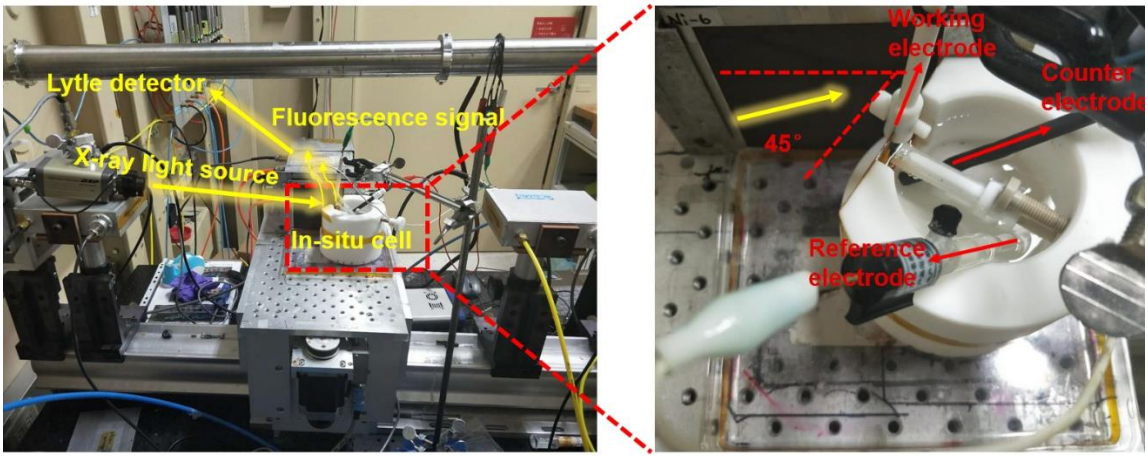

Figure S20. The detail of the *in-situ* XAS measurement.

For the in-situ XAS measurements, an electrochemical workstation and a custom-made poly tetra fluoroethylene cell equipped with a np-$Cu_{53}Ru_{47}$ working electrode, a graphite rod and a saturated calomel were used as counter electrode and reference electrode in 1.0 M KOH, respectively. The window of the cell was mounted at an angle of roughly 45° with respect to both the incident beam and the detector. All spectra of the samples were measured in fluorescence mode.

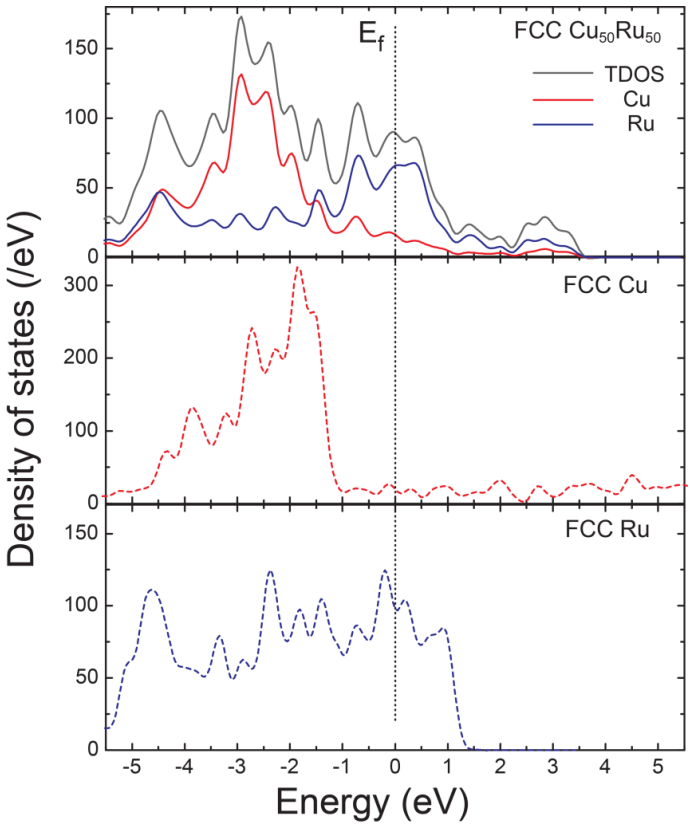

Figure S21. Local density of states projected for three metal surfaces.

Compared with the pure FCC Cu and Ru, the unoccupied electrons density of Cu at fermi-level increases after the incorporation of Ru atoms into the Cu matrix, while the electrons density of Ru decreases, which could be attributed to the electron transfer from Ru to Cu in after the incorporation of Ru atoms into the Cu matrix. This suggests that the alloying could effectively optimize the d-electron domination of Cu and Ru atoms, thus leading to enhanced HER perfomance.

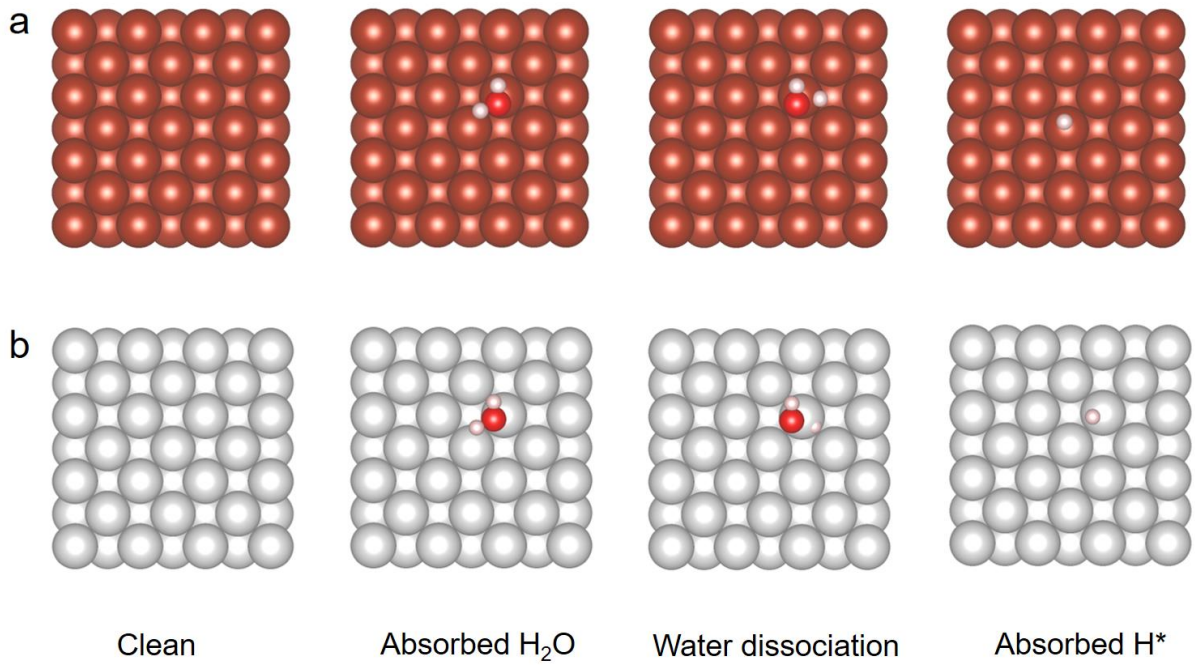

Figure S22. Atomic configurations of water dissociation step on the surface of pure Cu (a) and Ru (b). Color codes: deep orange, white represent of Cu and Ru. Red and light pink represent oxygen and hydrogen atoms in a single water molecule.

Table S1. ICP-OES analysis for $Ru_3Cu_{22}Mn_{75}$, np-Cu and np-$Cu_{53}Ru_{47}$.

	Element	wt%	at%
$Ru_3Cu_{22}Mn_{75}$	Cu	27.03	25.10
	Ru	7.11	4.15
	Mn	65.86	70.75
np-Cu	Cu	98.76	98.57
	Mn	1.24	1.43
np-$Cu_{53}Ru_{47}$	Cu	42.42	53.57
	Ru	56.53	44.89
	Mn	1.05	1.54

Table S2. Price of different noble metals[a]

Metal	Symbol	Unit of Measure	U.S.
Platinum	Pt	troy ounce	$974.00
Ruthenium	Ru	troy ounce	$195.00

[a] The prices for various noble metals are from the BASF corporation website on January 08, 2018.[4] (https://apps.catalysts.basf.com/apps/eibprices/mp/)

Table S3: Comparison of the surface parameters, mass activity and price activity for electrocatalysts investigated in 1.0 M KOH. Related to Figure 2.

Samples	C_{dl} (mF cm^{-2})	R_f^a	Surface area[b] (mA cm^{-2})	Mass activity[c] (mA mg^{-1})	Price activity[d] (A dollar^{-1})
np-$Cu_{53}Ru_{47}$	59	983.33	3212.21	199.599	29.018
Pt/C	97	1616.66	5281.08	81.085	2.36

a: the R_f was calculated by dividing C_{dl} by 0.06 mF cm^{-2}; b: the surface area was computed by multiplying the electrode geometrical area by R_f and then normalized by considering the loading mass of catalysts; c, d: the mass and price activity were got from the current density values of polarization curve at overpotential of 50 mV.[12]

Table S4. Comparison of the HER performance of catalysts in alkaline electrolyte.

Materials	Mass loading	Electrolyte	Overpotential at 10 mA/cm^2 (mV)	Tafel slope (mV/dec)	Ref.
np-$Cu_{53}Ru_{47}$	0.306 mg cm^{-2}	1.0 M KOH	15	30	This work
Ru/C_3N_4/C nanoparticle	/	0.1 M KOH	79	/	[13]
Ru@C_2N	0.285 mg cm^{-2}	1.0 M KOH	17	38	[14]
RuP_2@NPC (23.3wt%)	1.0 mg cm^{-2}	1.0 M KOH	52	69	[15]
Ru/CN	/	1.0 M KOH	21	31	[16]
RuCo@NC	0.275 mg cm^{-2}	1.0 M KOH	28	31	[17]
RuCoP	0.3 mg cm^{-2}	1.0 M KOH	23	37	[18]
Ni@Ni_2P-Ru HNRs	/	1.0 M KOH	41	31	[19]
Ru@GnP	0.25 mg cm^{-2}	1.0 M KOH	22	28	[20]

Rh_2P	0.153 mg cm^{-2}	1.0 M KOH	30	50	[21]
$Cu_{2-x}S$@Ru NPs	0.23 mg cm^{-2}	1.0 M KOH	82	48	[22]
Pt-$Co(OH)_2$/CC	6.9 (0.39 mg cm^{-2} for Pt)	1.0 M KOH	84	/	[23]
Co/CoP	0.88 mg cm^{-2}	1.0 M KOH	193	90.2	[24]
$Ru_{0.33}Se$ @ TNA	/	1.0 M KOH	57	50	[25]
Au–Ru-2 NWs	0.08 mg cm^{-2}	1.0 M KOH	50	30.8	[26]
Ni_3S_2@nanoporous Cu	/	1.0 M KOH	60.8	67.5	[27]
Ru_2Ni_2 SNs/C	0.1 mg cm^{-2}	1.0 M KOH	40	23.4	[28]
CoRu@NCs-2	0.273 mg cm^{-2}	1.0 M KOH	45	66	[29]
Ni-Mo	/	1.0 M KOH	35	45	[30]
Ni_5Co_3Mo-OH	/	1.0 M KOH	52	59	[31]
NiMoN	1.1 mg cm^{-2}	1.0 M KOH	109	95	[32]

Table S5. TOF values of np-$Cu_{53}Ru_{47}$ and some well-known HER catalysts in literatures.

Catalysts	Electrolyte	TOF (H_2 s^{-1}) (η=0.1 V)	References
np-$Cu_{53}Ru_{47}$	1.0 M KOH	1.139	This work
Sr_2RuO_4	1.0 M KOH	0.9	[4]
$NiCo_2P_x$	1.0 M KOH	0.056	[33]
Ni-MoS_2	1.0 M KOH	0.08	[34]
Ru/NG	1.0 M KOH	0.35	[35]
PtRu/RFCS	0.5 M H_2SO_4	0.375	[36]
Ni-Mo alloy	2.0 M KOH	0.05	[37]
S-CoO NRs	1.0 M KOH	0.41	[38]
Ni_5P_4	0.5 M H_2SO_4	0.06	[39]
$MoNi_4/MoO_2$@Ni	1.0 M KOH	0.4 (50 mV)	[40]

Table S6. Comparison of the HER performance of catalysts in neutral electrolyte.

Materials	Mass loading	Electrolyte	Overpotential at 10 $mAcm^{-2}$ (mV)	Tafel slope (mV dec^{-1})	Ref.
np-$Cu_{53}Ru_{47}$	0.306 mg cm^{-2}	1.0 PBS	41	35	This work
RuP_2@NPC	1.0 mg cm^{-2}	1.0 PBS	57	87	[15]
Rh_2P Nanoparticles	0.153mg cm^{-2}	1.0 PBS	38	46	[21]
Pt-$Co(OH)_2$/CC	0.39 mg cm^{-2} for Pt	1.0 PBS	32	70	[23]
Co/CoP	0.88 mg cm^{-2}	1.0 PBS	138	72.3	[24]
Ni_3S_2@nanoporous Cu	/	2.0 PBS	270	/	[27]
NiS_2/MoS_2 HNW	0.2 mg cm^{-2}	1.0 PBS	284	83	[41]
Ni-C-N NSs	0.2 mg cm^{-2}	1.0 PBS	92.1	38	[42]
$NiCo_2Px$/CF	5.9 mg cm^{-2}	1.0 PBS	63	63.3	[33]
$Ni_{0.33}Co_{0.67}S_2$/Ti foil	0.3 mg cm^{-2}	1.0 PBS	72	67.8	[43]
Co_9S_8@C	0.3 mg cm^{-2}	1.0 PBS	280	/	[44]

Table S7. The HER kinetic investigation in neutral and basic conditions. Gibbs free energies (G, eV) of adsorbed H_2O, H, and OH on the catalysts; the energy barriers (△G, eV) of H_2O dissociation step (Volmer step) and combination of H* into molecular hydrogen (Tafel step) on different catalyst models. Adsorption energy of H is referred to gas phase H_2.

Catalysts	G(H) (eV)	G(OH) (eV)	G (H_2O) (eV)	ΔG(H) (eV)	ΔG (H_2O) (eV)	ΔG(OH+H)(eV)	ΔG(OH) (eV)
Cu (001)	-0.974	-1.383	+1.936	1.041	-2.345	0.792	1.118
Ru (001)	-0.450	-1.131	-0.942	0.568	0.986	0.832	0.907
$Cu_{50}Ru_{50}$ (Cu sites)	-0.309	-1.102	+1.477	0.251	-1.416	0.928	1.069
$Cu_{50}Ru_{50}$ (Ru sites)	-0.185	-0.761	+0.840	0.092	-0.551	0.704	0.833

Table S8. Structural parameters extracted from the Cu K-edge Ru K-edge EXAFS fitting. (S_0^2=0.90)

	Path	R(Å)	N	$\sigma^2(10^{-3}Å^2)$	E_0(eV)	R factor
Ru	Ru-Cu	2.28	3.8	17.5	-17.639	0.006
	Ru-Ru	2.67	4.5	6.6	-5.694	
Cu	Cu-O	1.97	1.8	9.0	16.085	0.002
	Cu-Ru	2.63	3.2	6.3	0.607	
	Cu-Cu	2.43	4.1	10.5	-4.634	

S_0^2 is the amplitude reduction factor; CN is the coordination number; R is interatomic distance (the bond length between Cu, Ru central atoms and surrounding coordination atoms); σ^2 is Debye-Waller factor (a measure of thermal and static disorder in absorber-scatter distances); ΔE_0 is edge-energy shift (the difference between the zero kinetic energy value of the sample and that of the theoretical model). R factor is used to value the goodness of the fitting. This value was fixed during EXAFS fitting, based on the known structure of Cu metal and Ru metal.

References

(1). Jiang, K.; Liu, B.; Luo, M.; Ning, S.; Peng, M.; Zhao, Y.; Lu, Y. R.; Chan, T. S.; de Groot, F. M. F.; Tan, Y., Single Platinum Atoms Embedded in Nanoporous Cobalt Selenide as Electrocatalyst for Accelerating Hydrogen Evolution Reaction. *Nat. Commun.* **2019,** *10*, 1743.

(2). Xue, Y.; Huang, B.; Yi, Y.; Guo, Y.; Zuo, Z.; Li, Y.; Jia, Z.; Liu, H.; Li, Y., Anchoring Zero Valence Single Atoms of Nickel and Iron on Graphdiyne for Hydrogen Evolution. *Nat. Commun.* **2018**, *9*, 1460.

(3). Tiwari, J. N.; Sultan, S.; Myung, C. W.; Yoon, T.; Li, N.; Ha, M.; Harzandi, A. M.; Park, H. J.; Kim, D. Y.; Chandrasekaran, S. S.; Lee, W. G.; Vij, V.; Kang, H.; Shin, T. J.; Shin, H. S.; Lee, G.; Lee, Z.; Kim, K. S., Multicomponent Electrocatalyst with Ultralow Pt Loading and High Hydrogen Evolution Activity. *Nat. Energy.* **2018**, *3*, 773-782.

(4). Zhu, Y.; Tahini, H. A.; Hu, Z.; Dai, J.; Chen, Y.; Sun, H.; Zhou, W.; Liu, M.; Smith, S. C.; Wang, H.; Shao, Z., Unusual Synergistic Effect in Layered Ruddlesden-Popper Oxide Enables Ultrafast Hydrogen Evolution. *Nat. Commun.* **2019**, *10*, 149.

(5). Kibsgaard, J.; Tsai, C.; Chan, K.; Benck, J. D.; Nørskov, J. K.; Abild-Pedersen, F.; Jaramillo, T. F., Designing an Improved Transition Metal Phosphide Catalyst for Hydrogen Evolution Using Experimental and Theoretical Trends. *Energy Environ. Sci.* **2015**, *8*, 3022-3029.

(6). G. Kresse, J. Furthmüller, Efficient Iterative Schemes for Ab Initio Total-Energy Calculations Using a Plane-Wave Basis Set. *Phys. Rev. B* **1996**, *54*, 11169.

(7). G. Kresse, J. Furthmüller, Efficiency of Ab-Initio Total Energy Calculations for Metals and Semiconductors Using a Plane-Wave Basis Set. *Comput Mater Sci.* **1996**, *6*, 15.

(8). J. P. Perdew, K. Burke, M. Ernzerhof, Generalized Gradient Approximation Made Simple. *Phys. Rev. Lett.* **1996**, *77*, 3865.

(9). G. Kresse and D. Joubert, From Ultrasoft Pseudopotentials to the Projector Augmented-Wave Method. *Phys. Rev. B* **1999**, *59*, 1758-1775.

(10). Zhang, Q.; Kusada, K.; Wu, D.; Yamamoto, T.; Toriyama, T.; Matsumura, S.; Kawaguchi, S.; Kubota, Y.; Kitagawa, H., Selective control of FCC and HCP Crystal Structures in Au-Ru Solid-solution Alloy Nanoparticles. *Nat Commun.* **2018**, *9*, 510.

(11). Wang, F. L.; Kusada, K.; Wu, D. S.; Yamamoto, T.; Toriyama, T.; Matsumura, S.; Nanba, Y.; Koyama, M.; Kitagawa, H., Solid-Solution Alloy Nanoparticles of the Immiscible Iridium-Copper System with a Wide Composition Range for Enhanced Electrocatalytic Applications. *Angew. Chem. Int. Ed.* **2018,** *57*, 4505-4509.

(12). Shan, J.; Guo, C.; Zhu, Y.; Chen, S.; Song, L.; Jaroniec, M.; Zheng, Y.; Qiao, S.-Z., Charge-Redistribution-Enhanced Nanocrystalline Ru@IrO_x Electrocatalysts for Oxygen Evolution in Acidic Media. *Chem* **2019**, *5*, 445-459.

(13). Zheng, Y.; Jiao, Y.; Zhu, Y.; Li, L. H.; Han, Y.; Chen, Y.; Jaroniec, M.; Qiao, S. Z., High Electrocatalytic Hydrogen Evolution Activity of an Anomalous Ruthenium Catalyst. *J. Am. Chem. Soc.* **2016**, *138*, 16174-16181.

(14). Mahmood, J.; Li, F.; Jung, S. M.; Okyay, M. S.; Ahmad, I.; Kim, S. J.; Park, N.; Jeong, H. Y.; Baek, J. B., An Efficient and pH-Universal Ruthenium-Based Catalyst for the Hydrogen Evolution Reaction. *Nat. Nanotechnol.* **2017**, *12*, 441-446.

(15). Pu, Z.; Amiinu, I. S.; Kou, Z.; Li, W.; Mu, S., RuP_2 -Based Catalysts with Platinum-like Activity and Higher Durability for the Hydrogen Evolution Reaction at All pH Values. *Angew. Chem., Int. Ed.* **2017**, *56*, 11559-11564.

(16). Zhang, J.; Liu, P.; Wang, G.; Zhang, P. P.; Zhuang, X. D.; Chen, M. W.; Weidinger, I. M.; Feng, X. L., Ruthenium/Nitrogen-doped Carbon as an Electrocatalyst for Efficient Hydrogen Evolution in Alkaline Solution. *J. Mater. Chem. A* **2017**, *5*, 25314-25318.

(17). Su, J.; Yang, Y.; Xia, G.; Chen, J.; Jiang, P.; Chen, Q., Ruthenium-cobalt Nanoalloys Encapsulated in Nitrogen-doped Graphene as Active Electrocatalysts for Producing Hydrogen in Alkaline Media. *Nat. Commun.* **2017,** *8*, 14969.

(18). Xu, J.; Liu, T.; Li, J.; Li, B.; Liu, Y.; Zhang, B.; Xiong, D.; Amorim, I.; Li, W.; Liu, L., Boosting the Hydrogen Evolution Performance of Ruthenium Clusters Through Synergistic Coupling with Cobalt Phosphide. *Energy Environ. Sci.* **2018**,*11*, 1819-1827.
(19). Liu, Y.; Liu, S.; Wang, Y.; Zhang, Q.; Gu, L.; Zhao, S.; Xu, D.; Li, Y.; Bao, J.; Dai, Z., Ru Modulation Effects in the Synthesis of Unique Rod-like Ni@Ni_2P-Ru Heterostructures and Their Remarkable Electrocatalytic Hydrogen Evolution Performance. *J. Am. Chem. Soc.* **2018,** *140*, 2731-2734.
(20). Li, F.; H, G.-F.; Noh, H.-J.; Ahmad, I.; Jeon, I.-Y.; Baek, J.-B.; Mechanochemically Assisted Synthesis of a Ru Catalyst for Hydrogen Evolution with Performance Superior to Pt in Both Acidic and Alkaline Media. *Adv Mater.* **2018**, *30*,1803676.
(21). Yang, F.; Zhao, Y.; Du, Y.; Chen, Y.; Cheng, G.; Chen, S.; Luo, W., A Monodisperse Rh_2P-Based Electrocatalyst for Highly Efficient and pH-Universal Hydrogen Evolution Reaction. *Adv. Energy Mater.* **2018,** *8*, 1703489.
(22). Yoon, D.; Lee, J.; Seo, B.; Kim, B.; Baik, H.; Joo, S. H.; Lee, K., Cactus-Like Hollow $Cu_{2-x}S$@Ru Nanoplates as Excellent and Robust Electrocatalysts for the Alkaline Hydrogen Evolution Reaction. *Small* **2017,** *13*.1700052.
(23). Xing, Z.; Han, C.; Wang, D.; Li, Q.; Yang, X., Ultrafine Pt Nanoparticle-Decorated $Co(OH)_2$ Nanosheet Arrays with Enhanced Catalytic Activity toward Hydrogen Evolution. *ACS Catal.* **2017**, *7*, 7131-7135.
(24). Xue, Z.-H.; Su, H.; Yu, Q.-Y.; Zhang, B.; Wang, H.-H.; Li, X.-H.; Chen, J.-S., Janus Co/CoP Nanoparticles as Efficient Mott-Schottky Electrocatalysts for Overall Water Splitting in Wide pH Range. *Adv. Energy Mater*. **2017**, *7*, 1602355.
(25). Wang, K.; Chen, Q.; Hu, Y.; Wei, W.; Wang, S.; Shen, Q.; Qu, P., Crystalline $Ru_{0.33}Se$ Nanoparticles-Decorated TiO_2 Nanotube Arrays for Enhanced Hydrogen Evolution Reaction. *Small* **2018**, 1802132.
(26). Lu, Q.; Wang, A. L.; Gong, Y.; Hao, W.; Cheng, H.; Chen, J.; Li, B.; Yang, N.; Niu, W.; Wang, J.; Yu, Y.; Zhang, X.; Chen, Y.; Fan, Z.; Wu, X. J.; Chen, J.; Luo, J.; Li, S.; Gu, L.; Zhang, H., Crystal Phase-based Epitaxial Growth of Hybrid Noble Metal Nanostructures on 4H/fcc Au Nanowires. *Nat. Chem.* **2018,** *10*, 456-461.
(27). Yang, C.; Gao, M. Y.; Zhang, Q. B.; Zeng, J. R.; Li, X. T.; Abbott, A. P., In-situ Activation of Self-supported 3D Hierarchically Porous Ni_3S_2 Films Grown on Nanoporous Copper as Excellent pH-Universal Electrocatalysts for Hydrogen Evolution Reaction. *Nano Energy* **2017,** *36*, 85-94.
(28). Ding, J.; Shao, Q.; Feng, Y.; Huang, X., Ruthenium-Nickel Sandwiched Nanoplates for Efficient Water Splitting Electrocatalysis. *Nano Energy*. **2018**, *47*, 1-7.
(29). Xu, Y.; Li, Y.; Yin, S.; Yu, H.; Xue, H.; Li, X.; Wang, H.; Wang, L., Ultrathin Nitrogen-doped Graphitized Carbon shell Encapsulating CoRu Bimetallic Nanoparticles for Enhanced Electrocatalytic Hydrogen Evolution. *Nanotechnol.* **2018**, *29*, 225403.
(30). Zhang, Q.; Li, P.; Zhou, D.; Chang, Z.; Kuang, Y.; Sun, X., Superaerophobic Ultrathin Ni-Mo Alloy Nanosheet Array from In Situ Topotactic Reduction for Hydrogen Evolution Reaction. *Small* **2017**, *13*, 1701648.
(31). Hao, S.; Chen, L.; Yu, C.; Yang, B.; Li, Z.; Hou, Y.; Lei, L.; Zhang, X., NiCoMo Hydroxide Nanosheet Arrays Synthesized via Chloride Corrosion for Overall Water Splitting. *ACS Energy Letter.* **2019,** *4* , 952-959.
(32). Zhang, Y.; Ouyang, B.; Xu, J.; Chen, S.; Rawat, R. S.; Fan, H. J., 3D Porous Hierarchical Nickel-Molybdenum Nitrides Synthesized by RF Plasma as Highly Active and Stable Hydrogen-Evolution-Reaction Electrocatalysts. *Adv. Energy Mater.* **2016**, *6*, 1600221.
(33). Zhang, R.; Wang, X.; Yu, S.; Wen, T.; Zhu, X.; Yang, F.; Sun, X.; Wang, X.; Hu, W., Ternary $NiCo_2P_x$ Nanowires as pH-Universal Electrocatalysts for Highly Efficient Hydrogen Evolution Reaction. *Adv. Mater.* **2017**, *29*, 1605502.
(34). Zhang, J.; Wang, T.; Liu, P.; Liu, S.; Dong, R.; Zhuang, X.; Chen, M.; Feng, X., Engineering Water Dissociation Sites in MoS_2 Nanosheets for Accelerated Electrocatalytic Hydrogen Production. *Energy Environ. Sci*. **2016**, *9*, 2789-2793.

(35). Ye, R.; Liu, Y.; Peng, Z.; Wang, T.; Jalilov, A. S.; Yakobson, B. I.; Wei, S. H.; Tour, J. M., High Performance Electrocatalytic Reaction of Hydrogen and Oxygen on Ruthenium Nanoclusters. *ACS Appl. Mater. Interfaces* **2017**, *9*, 3785-3791.
(36). Li, K.; Li, Y.; Wang, Y.; Ge, J.; Liu, C.; Xing, W., Enhanced Electrocatalytic Performance for the Hydrogen Evolution Reaction through Surface Enrichment of Platinum Nanoclusters Alloying with Ruthenium in Situ Embedded in Carbon. *Energy Environ. Sci.* **2018**, *11*, 1232-1239.
(37). McKone, J. R.; Sadtler, B. F.; Werlang, C. A.; Lewis, N. S.; Gray, H. B., Ni–Mo Nanopowders for Efficient Electrochemical Hydrogen Evolution. *ACS Catal.* **2013**, *3*, 166-169.
(38). Ling, T.; Yan, D. Y.; Wang, H.; Jiao, Y.; Hu, Z.; Zheng, Y.; Zheng, L.; Mao, J.; Liu, H.; Du, X. W.; Jaroniec, M.; Qiao, S. Z., Activating Cobalt(II) Oxide Nanorods for Efficient Electrocatalysis by Strain Engineering. *Nat. Commun.* **2017,** *8*, 1509.
(39). Laursen, A. B.; Patraju, K. R.; Whitaker, M. J.; Retuerto, M.; Sarkar, T.; Yao, N.; Ramanujachary, K. V.; Greenblatt, M.; Dismukes, G. C., Nanocrystalline Ni_5P_4: a Hydrogen evolution Electrocatalyst of Exceptional Efficiency in both Alkaline and Acidic Media. *Energy Environ. Sci.* **2015**, *8*, 1027-1034.
(40). Zhang, J.; Wang, T.; Liu, P.; Liao, Z.; Liu, S.; Zhuang, X.; Chen, M.; Zschech, E.; Feng, X., Efficient Hydrogen Production on $MoNi_4$ Electrocatalysts with Fast Water Dissociation Kinetics. *Nat. Commun.* **2017,** *8*, 15437.
(41). Kuang, P.; Tong, T.; Fan, K.; Yu, J., In Situ Fabrication of Ni–Mo Bimetal Sulfide Hybrid as an Efficient Electrocatalyst for Hydrogen Evolution over a Wide pH Range. *ACS Catal.* **2017,** *7*, 6179-6187.
(42). Yin, J.; Fan, Q.; Li, Y.; Cheng, F.; Zhou, P.; Xi, P.; Sun, S., Ni-C-N Nanosheets as Catalyst for Hydrogen Evolution Reaction. *J. Am. Chem. Soc.* **2016,** *138*, 14546-14549.
(43). Peng, Z.; Jia, D.; Al-Enizi, A. M.; Elzatahry, A. A.; Zheng, G., From Water Oxidation to Reduction: Homologous Ni-Co Based Nanowires as Complementary Water Splitting Electrocatalysts. *Adv. Energy Mater.* **2015**, *5*, 1402031.
(44). Feng, L. L.; Li, G. D.; Liu, Y.; Wu, Y.; Chen, H.; Wang, Y.; Zou, Y. C.; Wang, D.; Zou, X., Carbon-Armored Co_9S_8 Nanoparticles as all-pH Efficient and Durable H_2-Evolving Electrocatalysts. *ACS Appl. Mater. Interfaces* **2015**, *7*, 980-988.